

# An Implicit Scheme for Ohmic Dissipation with Adaptive Mesh Refinement

Tomoaki MATSUMOTO

*Faculty of Humanity and Environment, Hosei University, Chiyoda-ku, Tokyo 102-8160, Japan*  
matsu@hosei.ac.jp

(Received 2010 September 4; accepted 2010 November 29)

## Abstract

An implicit method for the ohmic dissipation is proposed. The proposed method is based on the Crank–Nicolson method and exhibits second-order accuracy in time and space. The proposed method has been implemented in the SFUMATO adaptive mesh refinement (AMR) code. The multigrid method on the grids of the AMR hierarchy converges the solution. The convergence is fast but depends on the time step, resolution, and resistivity. Test problems demonstrated that decent solutions are obtained even at the interface between fine and coarse grids. Moreover, the solution obtained by the proposed method shows good agreement with that obtained by the explicit method, which required many time steps. The present method reduces the number of time steps, and hence the computational costs, as compared with the explicit method.

**Key words:** hydrodynamics — ISM: magnetic fields — magnetohydrodynamics: MHD — methods: numerical — stars: formation

## 1. Introduction

The magnetic field plays an important role in star formation. Taking the magnetic field into account, simulations of protostellar collapse have been performed in numerous studies (reviewed by Klein et al. 2007). Most of these studies assumed ideal magnetohydrodynamics (MHD).

Interstellar gas is partially ionized, and there are several processes of magnetic diffusion, e.g., the ohmic dissipation, the Hall effect, and ambipolar diffusion. The ohmic dissipation is effective at high densities of  $n \gtrsim 10^{16} \text{ cm}^{-3}$ , whereas the ambipolar diffusion is effective at low densities of  $n \lesssim 10^9 \text{ cm}^{-3}$  (e.g., Kunz & Balbus 2004). The timescale of the magnetic diffusion is significantly longer than the freefall time at  $n \lesssim 10^{12} \text{ cm}^{-3}$  (Nakano et al. 2002), and hence magnetic diffusion does not appear to change the behavior of the gravitational collapse qualitatively. The gravitational collapse ceases in the dense region of  $n \gtrsim 10^{11} \text{ cm}^{-3}$  owing to the formation of an adiabatic core, i.e., the first core (Larson 1969). Therefore, subsequently formed objects, e.g., circumstellar disks, protostars, and outflows, likely suffer from magnetic diffusion.

The recent numerical simulations for protostellar collapse begin to take into account the magnetic diffusion (e.g., Machida et al. 2006; Machida et al. 2007). However, the governing equation of the magnetic diffusion is parabolic, and therefore the time step for the magnetic diffusion is very small compared with the hydrodynamic time step when a high-resolution explicit method is employed. High resolution is important in the simulation of protostellar collapse and is usually provided by means of adaptive mesh refinement (AMR).

Several strategies for solving the magnetic diffusion have been proposed. The super time-stepping method is a type of explicit method, in which a large time step can be used (O’Sullivan & Downes 2006; O’Sullivan & Downes 2007; Choi et al. 2009). However, for the diffusion dominated problem, the time step is still restricted to be shorter than that of the hydrodynamic time step. Tilley & Balsara (2008) proposed a semi-implicit scheme for ambipolar diffusion using a two-fluid approximation, where the time step is restricted in inverse proportion to the drift velocity. The present author previously implemented the ohmic dissipation in a nested grid code by using a sub-cycle of the induction equation (Machida et al. 2006; Machida et al. 2007). By this method, the protostellar collapse from a molecular cloud core to protostar formation was successfully simulated. Although each sub-cycle required a small computational cost, the number of sub-cycles becomes very large when solving the magnetically dissipative region, e.g., the region proximal to and inside of a protostar. Moreover, the resistivity was approximated as being locally constant.

An implicit scheme for solving the ohmic dissipation has been developed and implemented in the SFUMATO MHD-AMR code (Matsumoto 2007). In §2, the details of the implicit scheme are presented. In §3, the results of several numerical tests are presented. Finally, the paper is summarized in §4.

## 2. Implicit scheme

The induction equation with the ohmic dissipation is given by

$$\frac{\partial \mathbf{B}}{\partial t} = \nabla \times (\mathbf{v} \times \mathbf{B} - \eta \nabla \times \mathbf{B}), \quad (1)$$

where  $\mathbf{B}$ ,  $\mathbf{v}$ , and  $\eta$  denote the magnetic field, velocity, and resistivity, respectively. Equation (1) is solved by an operator splitting approach. The contribution of the first term on the right-hand side of the equation is solved explicitly according to Matsumoto (2007), and the contribution of the second term is then solved by the implicit scheme presented herein. We hereinafter restrict our focus to the solution of the ohmic dissipation.

### 2.1. Discretization

The governing equation of the ohmic dissipation is given by

$$\frac{\partial \mathbf{B}}{\partial t} = -\nabla \times (\eta \nabla \times \mathbf{B}). \quad (2)$$

Equation (2) is written in conservation form as follows:

$$\frac{\partial \mathbf{B}}{\partial t} + \nabla \cdot \mathbf{F} = 0, \quad (3)$$

where the numerical flux  $\mathbf{F} = (\mathbf{F}_x, \mathbf{F}_y, \mathbf{F}_z)$  is given by

$$\mathbf{F}_x = \eta \begin{pmatrix} 0 \\ -\partial_x B_y + \partial_y B_x \\ -\partial_x B_z + \partial_z B_x \end{pmatrix}, \quad (4)$$

$$\mathbf{F}_y = \eta \begin{pmatrix} -\partial_y B_x + \partial_x B_y \\ 0 \\ -\partial_y B_z + \partial_z B_y \end{pmatrix}, \quad (5)$$

$$\mathbf{F}_z = \eta \begin{pmatrix} -\partial_z B_x + \partial_x B_z \\ -\partial_z B_y + \partial_y B_z \\ 0 \end{pmatrix}. \quad (6)$$

Equation (3) is discretized as follows:

$$\mathbf{B}_{i,j,k} - \mathbf{b}_{i,j,k} + \lambda \Delta t (\nabla \cdot \mathbf{F})_{i,j,k} + (1-\lambda) \Delta t (\nabla \cdot \mathbf{f})_{i,j,k} = 0, \quad (7)$$

where, for convenience, the unknown variables are written in uppercase, and the known variables are written in lowercase:  $\mathbf{B} := \mathbf{B}^{n+1}$ ,  $\mathbf{F} := \mathbf{F}^{n+1}$ ,  $\mathbf{b} := \mathbf{B}^n$ , and  $\mathbf{f} := \mathbf{F}^n$ . The superscript  $n$  denotes the time level, and  $\Delta t = t^{n+1} - t^n$ . The subscripts  $i, j, k$  are the indexes of a cell in the  $x, y$ , and  $z$  directions, respectively, and are used to label cells. The parameter  $\lambda$  specifies the type of temporal difference. The backward difference is obtained when  $\lambda = 1$ , and the central difference is obtained when  $\lambda = 1/2$ . Therefore,  $\lambda = 1$  results in a temporal first-order accuracy, while  $\lambda = 1/2$  results in a temporal second-order accuracy. The case of  $\lambda = 1/2$  corresponds to the Crank–Nicolson scheme. Spatial discretization is performed with the central difference, yielding spatial second-order accuracy. Each component of the numerical flux is defined at the cell surface, and hence the divergence of the numerical flux is calculated as follows:

$$\begin{aligned} (\nabla \cdot \mathbf{F})_{i,j,k} &= \frac{\mathbf{F}_{x,i+1/2,j,k} - \mathbf{F}_{x,i-1/2,j,k}}{\Delta x} \\ &+ \frac{\mathbf{F}_{y,i,j+1/2,k} - \mathbf{F}_{y,i,j-1/2,k}}{\Delta y} \\ &+ \frac{\mathbf{F}_{z,i,j,k+1/2} - \mathbf{F}_{z,i,j,k-1/2}}{\Delta z}, \end{aligned} \quad (8)$$

and  $(\nabla \cdot \mathbf{f})_{i,j,k}$  is calculated in the same manner. The differential terms in  $\mathbf{F}_{x,i+1/2,j,k}$  are given by

$$(\partial_x B_y)_{i+1/2,j,k} = \frac{B_{y,i+1,j,k} - B_{y,i,j,k}}{\Delta x}, \quad (9)$$

$$\begin{aligned} (\partial_y B_x)_{i+1/2,j,k} \\ = \frac{B_{x,i+1,j+1,k} + B_{x,i,j+1,k} - B_{x,i+1,j,k} - B_{x,i,j,k}}{2\Delta y}. \end{aligned} \quad (10)$$

The resistivity  $\eta$  at the cell surface is given by arithmetic average, e.g.,

$$\eta_{i+1/2,j,k} = \frac{\eta_{i+1,j,k} + \eta_{i,j,k}}{2}. \quad (11)$$

Equation (7) is rewritten in the form of a difference equation as follows:

$$\mathcal{L} \mathbf{B}_{i,j,k} = \mathbf{S}_{i,j,k}, \quad (12)$$

where

$$\mathcal{L} \mathbf{B}_{i,j,k} = \mathbf{B}_{i,j,k} + \lambda \Delta t (\nabla \cdot \mathbf{F})_{i,j,k}, \quad (13)$$

$$\mathbf{S}_{i,j,k} = \mathbf{b}_{i,j,k} - (1-\lambda) \Delta t (\nabla \cdot \mathbf{f})_{i,j,k}. \quad (14)$$

Equation (12) indicates that the unknown  $\mathbf{B}$  is solved by the linear operator  $\mathcal{L}$  and the source term  $\mathbf{S}$ , which is a function of the known  $\mathbf{b}$ .

### 2.2. Multigrid method

Equation (12) is solved by the multigrid method. Here, the strategy of the multigrid method is the same as that of Matsumoto (2007), who solved the scalar PDE of the Poisson equation, while the present method solves the vector PDE of equation (2). Therefore, all of the procedures of Matsumoto (2007) are extended to those for vectors, and full-weight prolongation and averaging restriction are performed for each vector component. Since the smoothing procedure depends on the equation to be solved, it is newly developed as shown in § 2.3.

The multigrid method  $\mathcal{L}_{\text{FMG}}^{-1}$  solves  $\mathbf{B}^{\text{new}}$  when the initial estimation  $\mathbf{B}^{\text{guess}}$  and the source term  $\mathbf{S}$  are given as follows:

$$\mathbf{B}^{\text{new}} = \mathcal{L}_{\text{FMG}}^{-1}(\mathbf{B}^{\text{guess}}, \mathbf{S}). \quad (15)$$

Since equation (12) is linear, we use the multigrid method iteratively, as follows:

$$\mathbf{R} = \mathbf{S} - \mathcal{L} \mathbf{B}^{\text{guess}} \quad (16)$$

$$\mathbf{B}^{\text{new}} = \mathbf{B}^{\text{guess}} + \mathcal{L}_{\text{FMG}}^{-1}(0, \mathbf{R}) \quad (17)$$

$$\mathbf{B}^{\text{guess}} \leftarrow \mathbf{B}^{\text{new}}. \quad (18)$$

This iterative utilization of the multigrid method reduces every component of a residual,  $\mathbf{R}$ .

The multigrid method given by equation (15) consists of (1) the full multigrid (FMG) cycle on the AMR hierarchical grids, (2) the multilevel adaptive technique (MLAT) with the full approximation scheme (FAS) on these grids, and (3) an FMG-cycle on the base grid (Matsumoto 2007). These schemes have parameters: the numbers of iterations for V-cycle, pre-smoothing, and post-smoothing procedures in each grid level. These parameters adopted

**Table 1.** Numbers of iterations for the multigrid method

Schemes	V-cycle	Pre-smoothing	Post-smoothing
FMG on AMR	4	4	4
MLAT-FAS on AMR	2	4	4
FMG on base grid	2	2	2

through this paper are shown in table 1. These parameters affect a convergence speed of the multigrid method; small numbers of these iterations slow the convergence while the computational cost is reduced.

As shown in section 3, several cycles of the multigrid method given by equations (16)–(18) reduce the residual by more than an order of magnitude. In the numerical tests, we performed 20 cycles of the multigrid method in order to estimate solutions converged enough.

### 2.3. Smoothing

As a smoothing operator, the red-black Gauss–Seidel iteration is adopted. When equation (12) is solved separately for  $\mathbf{B}_{i,j,k}$  in each vector component, and  $\mathbf{B}_{i,j,k}$  is replaced by  $\mathbf{B}_{i,j,k}^{\text{updated}}$ , we obtain the following relationship:

$$\mathbf{B}_{i,j,k}^{\text{updated}} = \mathbf{B}_{i,j,k} + \begin{pmatrix} R_{x,i,j,k}/(1 + \alpha_x) \\ R_{y,i,j,k}/(1 + \alpha_y) \\ R_{z,i,j,k}/(1 + \alpha_z) \end{pmatrix}, \quad (19)$$

where

$$\mathbf{R}_{i,j,k} = \begin{pmatrix} R_{x,i,j,k} \\ R_{y,i,j,k} \\ R_{z,i,j,k} \end{pmatrix} = \mathbf{S}_{i,j,k} - \mathcal{L}\mathbf{B}_{i,j,k}, \quad (20)$$

$$\alpha_x = \lambda\Delta t \left( \frac{\eta_{i,j-1/2,k} + \eta_{i,j+1/2,k}}{\Delta y^2} + \frac{\eta_{i,j,k-1/2} + \eta_{i,j,k+1/2}}{\Delta z^2} \right), \quad (21)$$

$$\alpha_y = \lambda\Delta t \left( \frac{\eta_{i,j,k-1/2} + \eta_{i,j,k+1/2}}{\Delta z^2} + \frac{\eta_{i-1/2,j,k} + \eta_{i+1/2,j,k}}{\Delta x^2} \right), \quad (22)$$

$$\alpha_z = \lambda\Delta t \left( \frac{\eta_{i-1/2,j,k} + \eta_{i+1/2,j,k}}{\Delta x^2} + \frac{\eta_{i,j-1/2,k} + \eta_{i,j+1/2,k}}{\Delta y^2} \right). \quad (23)$$

Equation (19) gives the approximate solution of  $\mathbf{B}_{i,j,k}^{\text{updated}}$  for a given initial guess of  $\mathbf{B}_{i,j,k}$ . We adopt equation (19) as a smoothing operator. A red-black ordering is adopted for sweeping the grid.

### 2.4. Time step

The AMR code was equipped with two modes of time-marching: an adaptive and a synchronous time-step mode. In the former mode, a coarser grid has a longer time step

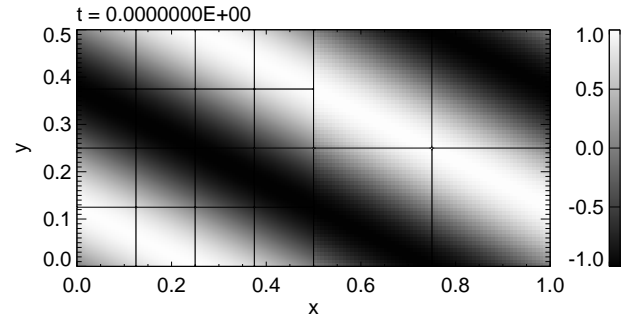


**Fig. 1.** Initial condition for the sinusoidal diffusion problem. The gray scale denotes the distribution of  $B_z$ , and lines denote the boundaries of the AMR blocks, each of which has  $32^3$  cells.

than a finer grid, and this mode is appropriate for non-self-gravitational gases because the system equations are hyperbolic. In the latter mode, every grid-level has the same time step, and this mode is appropriate for self-gravitational gases because the Poisson equation is elliptic. For a problem including the ohmic dissipation, the synchronous time-step is adopted because the equation (2) is parabolic.

## 3. Numerical tests

### 3.1. Sinusoidal diffusion problem

We consider the problem in which the sinusoidal magnetic field diffuses with a constant resistivity. The initial magnetic field is given as follows:

$$B_z = \sin(\mathbf{k} \cdot \mathbf{r}), \quad (24)$$

and  $B_x = B_y = 0$ , where the wave number is set at  $\mathbf{k} = 2\pi(1, 2, 0)^T$ . This setting reduces the equation of the ohmic dissipation to the heat equation. The resistivity is set at  $\eta = 1$ . The computational domain is  $x, y, z \in [0, 1] \times [0, 1/2] \times [0, 1/4]$ . Periodic boundary conditions are imposed. The computational domain is covered by  $4 \times 2 \times 1$  base blocks, each of which has  $N^3$  cubic cells. The cell width is therefore given by  $\Delta x = \Delta y = \Delta z = 1/(4N)$  in the base grid. The domain of  $x \in [0, 1/2]$  is refined by blocks that are twice as fine. Figure 1 shows the initial distribution of  $B_z$  and the block distribution for  $N = 32$ . The cell width in the left-hand side is  $\Delta x = 1/256$ , and that in the right-hand side is  $\Delta x = 1/128$ .

We performed the convergence test by changing the time step  $\Delta t$ , in order to measure the temporal accuracy. The  $L_1$  norm of the error is measured at  $t = 4 \times 10^{-3}$  through comparison with the exact solution of the following equation:

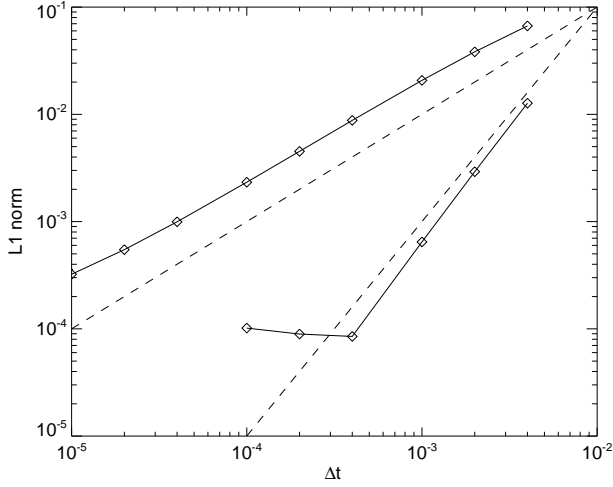


**Fig. 2.**  $L_1$  norm of error as a function of time step  $\Delta t$  for the sinusoidal diffusion problem. The spatial resolution is  $N = 32$ . The upper and lower solid lines denote the errors for the cases in which  $\lambda = 1$  and  $1/2$ , respectively. The dashed lines indicate the relationships of errors in proportion to  $\Delta t$  and  $\Delta t^2$ , respectively.

$$B_{\text{ex}}(\mathbf{r}) = \exp(-\eta|\mathbf{k}|^2 t) \sin(\mathbf{k} \cdot \mathbf{r}). \quad (25)$$

The  $L_1$  norm is estimated as follows:

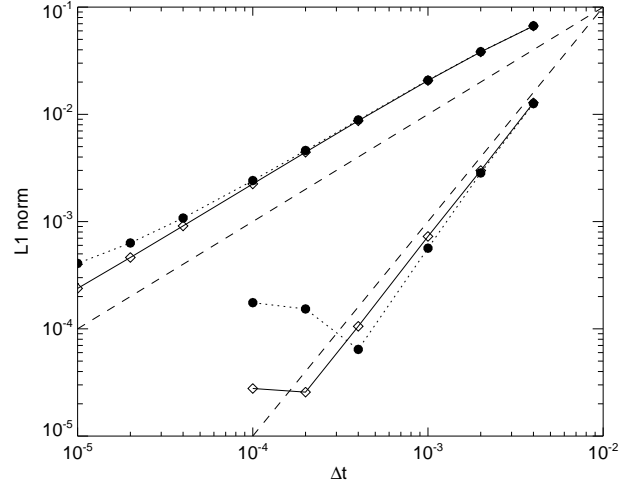
$$L_1 = \frac{1}{V} \sum_{i,j,k} |B_z(\mathbf{r}_{i,j,k}) - B_{\text{ex}}(\mathbf{r}_{i,j,k})| \Delta V_{i,j,k}, \quad (26)$$

where  $\Delta V_{i,j,k}$  denotes the volume of a cell located at  $\mathbf{r}_{i,j,k}$ , and  $V$  denotes the volume of the entire computational domain. By the stage of  $t = 4 \times 10^{-3}$ , the amplitude of  $B_z$  is reduced to 0.45.

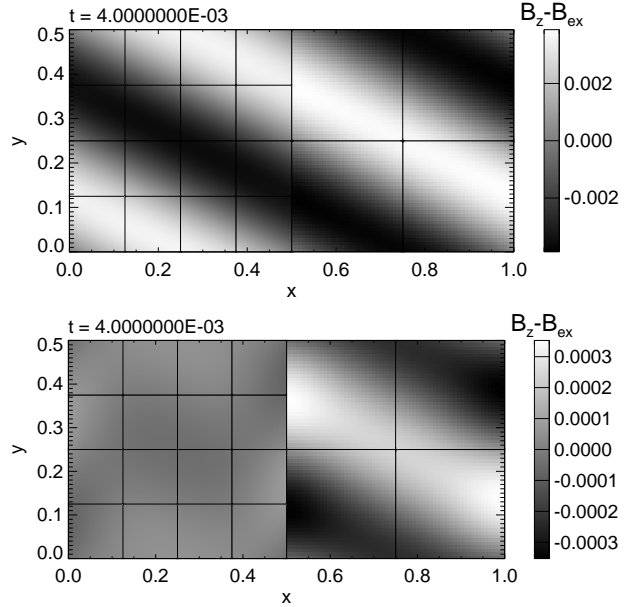
Figure 2 shows the  $L_1$  norm as a function of the time step  $\Delta t$ . We examined the cases of  $\lambda = 1$  (backward difference) and  $\lambda = 1/2$  (Crank–Nicolson). The scheme with  $\lambda = 1$  exhibits first-order accuracy, and that with  $\lambda = 1/2$  exhibits second-order accuracy. For the scheme with  $\lambda = 1/2$ , the decrease in the  $L_1$  norm with decreasing  $\Delta t$  is saturated at  $\Delta t \leq 2 \times 10^{-4}$ , exhibiting the constant  $L_1$  norm of  $\sim 10^{-4}$ . The saturation is primarily attributed to a discretization error. We confirmed that the value of the saturation decreases with decreasing cell width.

Figure 3 shows the  $L_1$  norms estimated in the fine region of  $0 \leq x < 1/2$  (fine region) and the coarse region of  $1/2 < x \leq 1$  (coarse region). For the first-order scheme ( $\lambda = 1$ ), the error in the coarse grid is slightly larger than that in the fine grid. In contrast, the second-order scheme ( $\lambda = 1/2$ ) exhibits an error in the coarse grid that is approximately 6 times larger than that in the fine grid when  $\Delta t \leq 2 \times 10^{-4}$ .

Figure 4 shows the distributions of the errors at  $\Delta t = 10^{-4}$  for the schemes with  $\lambda = 1$  and  $1/2$ . For the first-order scheme ( $\lambda = 1$ ), the error is distributed smoothly through the fine and coarse grids. For the second-order scheme ( $\lambda = 1/2$ ), the coarse grid shows a larger systematic error than the fine grid, causing the large  $L_1$  norm in the coarse grid. Moreover, the error is somewhat large in the coarse grid near the interface between the fine and coarse



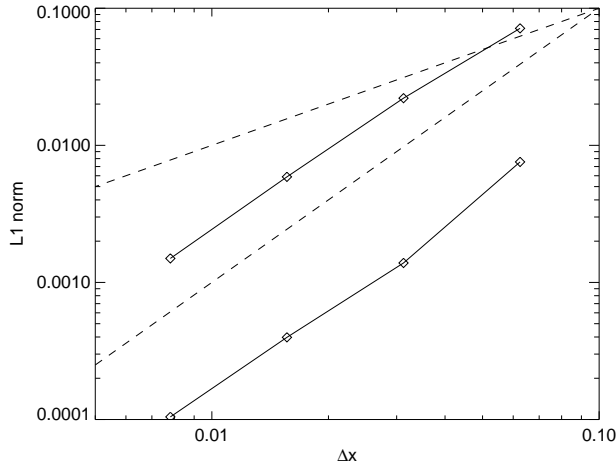
**Fig. 3.**  $L_1$  norm of error as a function of time step  $\Delta t$  for the sinusoidal diffusion problem. The spatial resolution is  $N = 32$ . The upper and lower lines denote the errors for the cases in which  $\lambda = 1$  and  $1/2$ , respectively. The solid lines with diamonds and the dotted lines with filled circles denote the errors in  $x \in [0, 1/2]$  (fine region) and  $x \in (1/2, 1]$  (coarse region), respectively. The dashed lines indicate the relationships of errors in proportion to  $\Delta t$  and  $\Delta t^2$ .



**Fig. 4.** Distribution of error  $B_z - B_{\text{ex}}$  in the  $x - y$  plane for the sinusoidal diffusion problem. Errors are shown for the  $N = 32$  resolution and  $\Delta t = 10^{-4}$ , solved by a scheme with  $\lambda = 1$  (upper) and a scheme that with  $\lambda = 1/2$  (lower).

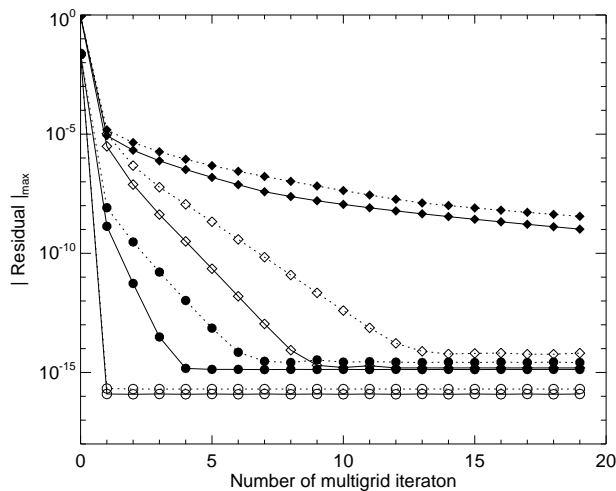
grids.

Figure 6 shows the decrease in the maximum residual during the iteration of the multigrid method given by equations (16) through (18) for various time steps  $\Delta t$  and spatial resolutions  $N$ . The residual is calculated according to equation (20), and  $\max(|R_{x,i,j,k}|, |R_{y,i,j,k}|, |R_{z,i,j,k}|)$  is plotted. In all cases, one iteration of the multigrid method reduces the residual to less than  $10^{-5}$ . Comparison of



**Fig. 5.**  $L_1$  norm of error as a function of cell width  $\Delta x$  for the sinusoidal diffusion problem. Upper and lower solid lines indicate the errors obtained by the schemes with  $\lambda = 1$  and  $1/2$ , respectively. The dashed lines indicate the relationships of errors in proportion to  $\Delta t$  and  $\Delta t^2$ .

We performed a convergence test with respect to the spatial resolution by changing the number of cells inside a block,  $N^3 = 4^3, 8^3, 16^3, 32^3$ . The time step is set to  $\Delta t = 4 \times 10^{-3}(4/N)^2$ . Figure 5 shows the  $L_1$  norm as a function of the cell width  $\Delta x$  for the schemes with  $\lambda = 1$  and  $1/2$ . Both schemes exhibit spatial second-order accuracy.



**Fig. 6.** Maximum residual  $|R|_{\max}$  as a function of iteration number of the multigrid method for the sinusoidal diffusion problem. Solid and dotted lines indicate data for  $\lambda = 1/2$  and  $1$ , respectively. Diamonds and circles indicate data for  $\Delta t = 4 \times 10^{-3}$  and  $10^{-4}$ , respectively. Open and filled symbols indicate data for  $N = 8$  and  $32$ , respectively.

the schemes with  $\lambda = 1/2$ , and  $1$  reveals that the scheme with  $\lambda = 1/2$  exhibits fast convergence. Moreover, there is a tendency whereby cases with smaller  $\eta\Delta t/\Delta x^2$  exhibit faster convergence. The residuals with  $\eta\Delta t/\Delta x^2 = 262, 16.4, 6.55$ , and  $0.410$  in the fine grid correspond to the lines with filled diamonds, open diamonds, filled circles,

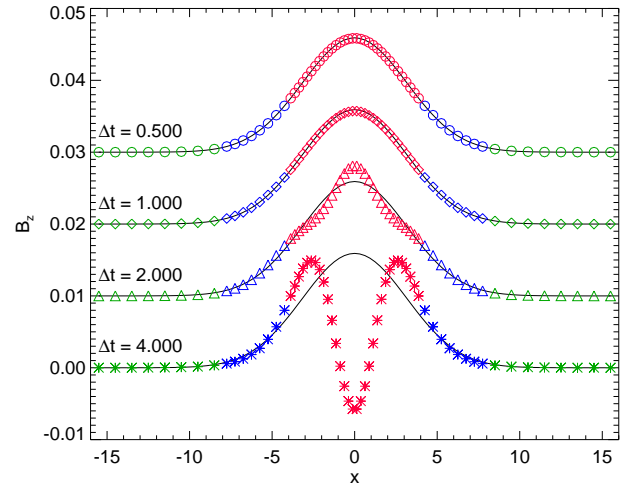


**Fig. 7.** Distribution of  $B_z$  in the  $y = 0$  plane at  $t = 4$  for the Gaussian diffusion problem with  $\lambda = 1/2$ . Circles, diamonds, triangles, and asterisks denote the solutions of  $\Delta t = 0.5$ ,  $1.0$ ,  $2.0$ , and  $4.0$ , respectively. Green, blue, and red symbols indicate solutions on the grids of levels 0, 1, and 2, respectively. The solid curve denotes the exact solution. In order that all of the solutions could be plotted, the plots are offset from each other by  $0.01$  in the vertical direction.

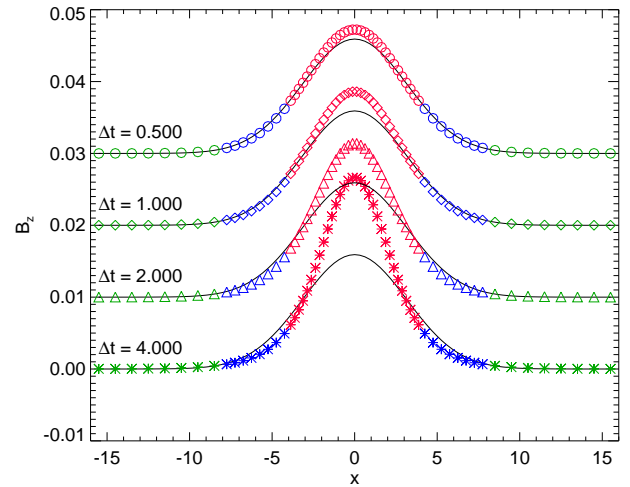


**Fig. 8.** Same as Figure 7, but for  $\lambda = 1$ .

and open circles, respectively.

### 3.2. Gaussian diffusion problem

We examine the diffusion of  $B_z$  in the Gaussian profile, the exact solution of which is given as follows:

$$B_z(x, y) = \frac{1}{4\pi\eta(t+t_0)} \exp\left[-\frac{x^2+y^2}{4\eta(t+t_0)}\right] \quad (27)$$

where  $t_0 = 1$  and  $\eta = 1$ . The computational domain is  $x, y, z \in [-16, 16]$ , which is resolved by the base grid of  $32^3$  cubic cells. The region around the  $z$  axis ( $x = y = 0$ ) is covered by the fine grids, as shown in Figure 7. The cell widths are  $\Delta x = 1.0, 0.5$ , and  $0.25$  for the grids of levels 0, 1, and 2, respectively. Periodic boundary conditions are imposed.



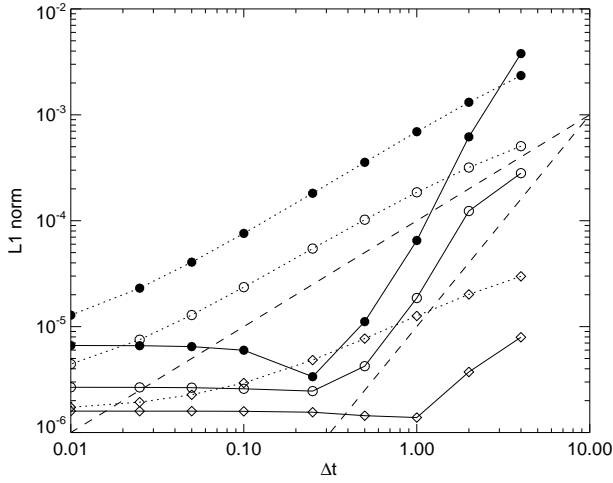


**Fig. 9.**  $L_1$  norm of error as a function of time step  $\Delta t$  for the Gaussian diffusion problem. Solid and dotted lines indicate the errors obtained by the schemes with  $\lambda = 1/2$  and 1, respectively. Diamonds, open circles, and filled circles denote the errors on the grids of levels 0, 1, and 2, respectively. The dashed lines indicate the relationships of errors in proportion to  $\Delta t$  and  $\Delta t^2$ .

Figure 7 shows the solutions of  $B_z$  at  $t = 4$  with various time steps  $\Delta t$  for the scheme of  $\lambda = 1/2$ . As the time step  $\Delta t$  increases, the solution deviates from the exact solution. The solution with  $\Delta t = 2.0$  shows significant undulation  $|x| \lesssim 4$ . For the solution with  $\Delta t = 4.0$ , the undulation mashes up the solution in the finest grid (red asterisks). Note that the Crank–Nicolson method is unconditionally stable for the von Neumann stability analysis, while a large  $\eta\Delta t/\Delta x^2$  produces such undulation due to violation of the maximum principle (Morton & Mayer 2005). We also found that the undulation occurred with smaller  $\Delta t$  when the initial Gaussian profile had a narrower width (a smaller  $t_0$ ).

The scheme with  $\lambda = 1$  yields smooth solutions even for large  $\Delta t$ , as shown in Figure 8. Although monotonicity is maintained in the solutions, the solution in the finest grid deviated considerably from the exact solution when  $\Delta t$  is large.

Figure 9 shows the  $L_1$  norm of the error as a function of time step  $\Delta t$  for  $\lambda = 1/2$  (solid lines) and 1 (dotted lines). The norm is estimated separately on each grid level. The errors for  $\lambda = 1/2$  and 1 exhibit second-order accuracy and first-order accuracy, respectively, on the grids of levels 1 and 2. For the grid of level 0 (the base grid), the dependence of the errors on  $\Delta t$  is shallower because of the periodic boundary conditions. Note that the scheme with  $\lambda = 1/2$  maintains second-order accuracy on the grid of level 2, even when considerable undulation occurs with a large time step.

### 3.3. Comparison with an explicit scheme

We compared the solutions obtained by implicit schemes with the solutions obtained by an explicit scheme. The resistivity is distributed as follows:

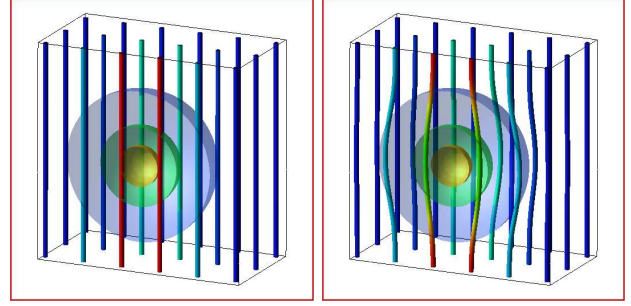


**Fig. 10.** Distributions of the magnetic field  $\mathbf{B}$  and the resistivity  $\eta$  at the initial stage (left) and the stage of  $t = 1$  (right), which is solved by the second-order implicit scheme with  $\lambda = 1/2$ . Tubes and isosurfaces denote the magnetic field lines and resistivity, respectively. The colors of tubes illustrate the field strength. The levels of the isosurfaces are  $\eta = 0.05, 0.425, 0.8$ . The region of  $x, z \in [-2.4, 2.4]$ ,  $y \in [0, 2.4]$  is shown.

$$\eta(\mathbf{r}) = \exp[-(x^2 + y^2 + z^2)] \quad (28)$$

and the initial magnetic field is given by

$$B_z(\mathbf{r}) = \exp[-(x^2 + y^2)] \quad (29)$$

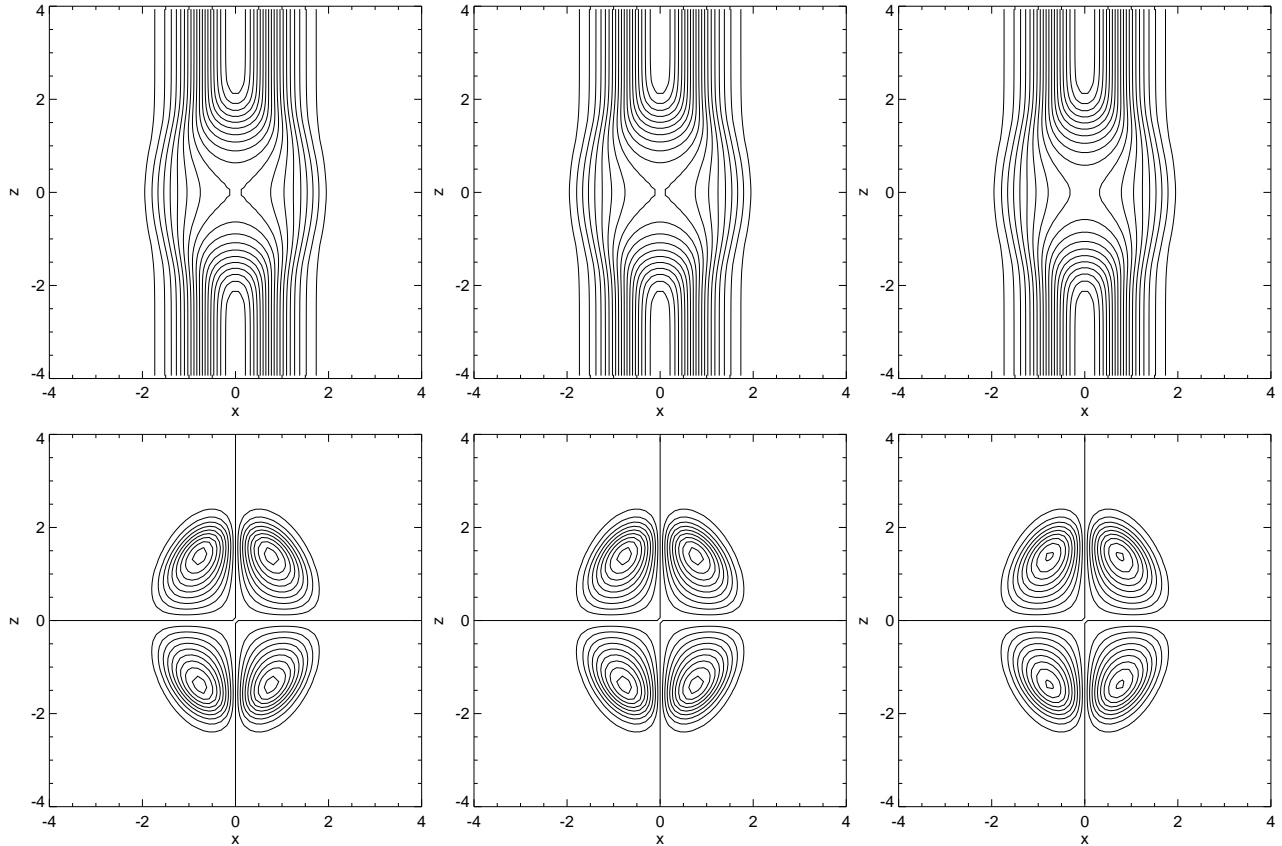
and  $B_x = B_y = 0$ . The computational domain is  $x, y, z \in [-4, 4]$ , which is resolved by  $64^3$  cells. Periodic boundary conditions are imposed. We continue the dissipation process of  $\mathbf{B}$  until  $t = 1$  by using the implicit schemes with  $\lambda = 1/2$  and 1 and an explicit scheme. The explicit scheme integrates time by means of the predictor-corrector method and a spatial central difference in order to achieve second-order accuracy in time and space. The time step is set at  $\Delta t = 10^{-3}$  for the explicit scheme, and  $\Delta t = 10^{-1}$  for the implicit schemes.

Figure 10 shows the initial conditions and the solution at  $t = 1$  solved by the implicit scheme with  $\lambda = 1/2$ . The right-hand figures show the magnetic fields bent due to the ohmic dissipation, indicating the reduction of  $B_z$  and the generation of  $B_x$  and  $B_y$ .

Figure 11 compares magnetic fields obtained by the explicit scheme, the second-order implicit scheme ( $\lambda = 1/2$ ), and the first-order implicit scheme ( $\lambda = 1$ ). All of the solutions are consistent with one another. In particular, the solution obtained by the implicit scheme with  $\lambda = 1/2$  exhibits excellent agreement with that obtained by the explicit scheme. This is attributed to the high accuracy of the implicit scheme with  $\lambda = 1/2$ , which achieves second-order accuracy.

## 4. Summary and Discussion

We have presented an implicit scheme for solving the ohmic dissipation for the SFUMATO MHD-AMR code. The induction equation of the ohmic dissipation is solved by this implicit scheme, which is based on the Crank–Nicolson method, which has an option for selecting first-order accuracy ( $\lambda = 1$ ) and second-order accuracy ( $\lambda = 1/2$ ) in time. For both cases, the spatially central difference yields second order accuracy in space.



**Fig. 11.** Distributions of the magnetic fields at  $t = 1$  in the  $y = 0$  plane. The magnetic fields are solved by the explicit scheme (*left*), the implicit scheme with  $\lambda = 1/2$  (*middle*), and the implicit scheme with  $\lambda = 1$  (*right*). Upper panels show  $B_z$ , where the contour levels are  $B_z = 0.05, 0.1, \dots, 0.95$ . Lower panels show  $B_x$ , where the contour levels are  $B_x = -0.09, -0.08, \dots, 0.09$ .

The multigrid method is used for the convergence of a solution and exhibits fast convergence. Although the convergence speed depends on  $\eta\Delta t/\Delta x^2$ , several cycles of the multigrid method reduce the residual by more than an order magnitude. The solution is obtained over the AMR hierarchical grid, in which fine and coarse grids coexist. Moreover, no spurious features appear at the interface between fine and coarse grids. Note that in the convergence process of the multigrid method, the numerical fluxes given by equations (4) through (6) are conserved even at the interfaces between the fine and coarse grids, because of the refluxing procedure, where the fluxes of the coarse grid are obtained by summing those of the fine grids at the interface (Matsumoto 2007). This leads to conservation of magnetic flux.

Since the second-order scheme of  $\lambda = 1/2$  is based on the Crank–Nicolson method, the scheme is unconditionally stable. However, the solution can contain spurious oscillations when  $\eta\Delta t/\Delta x^2$  is large, as shown in Figure 7. For example, for a one-dimensional heat equation, the analysis of the maximum principle leads a condition of  $\eta\Delta t/\Delta x^2 \leq 3/2$  to suppress the oscillation (Morton & Mayer 2005). This condition is slightly weaker than the CFL condition of an explicit scheme. In the astrophysical simulations, the oscillation of the magnetic field may change the direction of the magnetic pressure gradient,

which may change the phenomena of the simulations qualitatively. In contrast, the first-order scheme ( $\lambda = 1$ ) retains monotonicity, as shown in Figure 8, but its error is larger than that of the second-order scheme.

Numerical computations were carried out on the Cray XT4 at the Center for Computational Astrophysics, CfCA, of the National Astronomical Observatory of Japan. The present research was supported in part by the Hosei Society of Humanity and Environment. The present research was supported in part by Grants-in-Aid for Scientific Research (C) 20540238 and (B) 22340040 from the Ministry of Education, Culture, Sports, Science and Technology, Japan.

## References

- Choi, E., Kim, J., & Wiita, P. J. 2009, *ApJS*, 181, 413
- Klein, R. I., Inutsuka, S.-I., Padoan, P., & Tomisaka, K. 2007, *Protostars and Planets V*, 99
- Kunz, M. W., & Balbus, S. A. 2004, *MNRAS*, 348, 355
- Larson, R. B. 1969, *MNRAS*, 145, 271
- Machida, M. N., Inutsuka, S.-i., & Matsumoto, T. 2006, *ApJL*, 647, L151
- Machida, M. N., Inutsuka, S.-i., & Matsumoto, T. 2007, *ApJ*, 670, 1198
- Matsumoto, T. 2007, *PASJ*, 59, 905

- Morton K. W. & Mayers D. F. 2005, Numerical solution of partial differential equations: an introduction (Cambridge University Press) page33
- Nakano, T., Nishi, R., & Umebayashi, T. 2002, ApJ, 573, 199
- O'Sullivan, S., & Downes, T. P. 2006, MNRAS, 366, 1329
- O'Sullivan, S., & Downes, T. P. 2007, MNRAS, 376, 1648
- Tilley, D. A., & Balsara, D. S. 2008, MNRAS, 389, 1058